Classical trajectory and statistical adiabatic channel study of the dynamics of capture and unimolecular bond fission. IV. Valence interactions between atoms and linear rotors

A. I. Maergoiz, E. E. Nikitin, J. Troe, and V. G. Ushakov

Citation: The Journal of Chemical Physics **108**, 5265 (1998); doi: 10.1063/1.475963
View online: http://dx.doi.org/10.1063/1.475963
View Table of Contents: http://scitation.aip.org/content/aip/journal/jcp/108/13?ver=pdfcov
Published by the AIP Publishing

Classical trajectory and statistical adiabatic channel study of the dynamics of capture and unimolecular bond fission. IV. Valence interactions between atoms and linear rotors

A. I. Maergoiz,[a] E. E. Nikitin,[b] J. Troe,[c] and V. G. Ushakov[d]
Institut für Physikalische Chemie, Universität Göttingen, Tammannstrasse 6, D-37077 Göttingen, Germany

(Received 23 April 1997; accepted 24 December 1997)

The addition of atoms to linear molecules forming linear or nonlinear adducts is treated using standardized valence potentials. The dynamics is analyzed with a combination of classical trajectory (CT) and statistical adiabatic channel (SACM) calculations. For classical adiabatic conditions, the two approaches coincide. The transition from adiabatic to nonadiabatic dynamics is investigated using CT calculations. The low-temperature adiabatic quantum range is studied by SACM. Thermal capture rate constants are represented in analytical form. Thermal rigidity factors are expressed in terms of molecular parameters such as the frequencies of transitional bending modes, the bond dissociation energy, the rotational constant of the linear fragment, and the ratio of the looseness and Morse parameters α/β of the potential-energy surface. The final rate expressions are of simple form suitable for direct practical applications. © *1998 American Institute of Physics.* [S0021-9606(98)01113-1]

I. INTRODUCTION

In parts I–III of this series we have analyzed the capture of ions by dipoles,[1] by quadrupoles,[2] and of dipoles by dipoles,[3] comparing rigorous applications[4] of the statistical adiabatic channel model (SACM)[5] with extensive classical trajectory (CT) calculations. It was shown that the two treatments agree completely in the range of classical adiabatic dynamics. In the low-temperature quantum range only SACM is applicable. Ion–dipole and ion–quadrupole capture show nonadiabatic dynamics only at very high temperatures, the CT treatment allowing for an analytical representation of the transition between adiabatic and nonadiabatic (sudden) capture rate constants.[1,2] The situation is more complex for dipole–dipole capture[3,6–8] where numerous simple and multiple Landau–Zener type avoided crossings between higher adiabatic channel potential curves are encountered and transitions between adiabatic and nonadiabatic capture dynamics of different types have to be considered for higher temperatures.

The combined SACM and CT treatment of Refs. 1–3 allowed for an analytical representation of the thermal capture rate constants in terms of molecular parameters. It appeared promising to also apply the mentioned approach to short-range valence potentials. One may hope to again obtain compact analytical expressions for capture or the corresponding dissociation rate constants. First attempts on a crude level have been made earlier,[9–11] using simplified oscillator versions of SACM, and employing simple anisotropy models of valence potentials.[12] In the present work, this concept will be followed on a more rigorous level. We derive SACM and CT capture rate constants for atoms combining with linear species, using simple Morse-type attraction potentials and simple anisotropy models for the valence potential. The capture rate constants are again expressed analytically in terms of the relevant molecular parameters. One should keep in mind that real potentials may be more complicated, showing nonsmooth transitions between short-range valence and long-range electrostatic components (see, e.g., the H_2O_2 system in Ref. 13). However, the present results serve as a useful reference for comparison, in particular because an increasing number of high-pressure association measurements is becoming available now (see summaries in Refs. 9 and 14–16). Capture rates are also interesting because they provide upper limits for rate constants of complex-forming bimolecular reactions.[17]

Classical trajectory calculations of thermal capture (or the reverse thermal dissociation) rate constants on valence potential-energy surfaces obviously have frequently been done before. Recent reviews and exemplary calculations for specific molecular systems such as Refs. 18–21 describe the state of the methodology and the dynamic features calculated. The present treatment differs from these studies in some aspects: (i) the influence of key properties of the potential is elaborated systematically such that capture rate constants can be expressed in analytical form as a function of few molecular parameters, (ii) the coincidence of SACM and CT under classical adiabatic conditions is verified, (iii) the transition from classical adiabatic to nonadiabatic dynamics is quantified, and (iv) explicit rate coefficients for low-temperature quantum adiabatic capture are elaborated. We do these calculations for situations with linear and nonlinear adduct formation. The addition of two linear species forming

[a]On leave from N. N. Semenov Institute of Chemical Physics, Russian Academy of Sciences, 117977, Moscow.
[b]Department of Chemistry, Technion-Israel Institute of Technology, Haifa, 32000, Israel.
[c]Author to whom correspondence should be addressed.
[d]Institute of Chemical Physics, Russian Academy of Sciences, 142432 Chernogolovka.

linear or nonlinear adducts will be treated in a subsequent article[22] (part V of this series).

II. REDUCED HAMILTONIAN AND MASSEY PARAMETER

Following the concepts of parts I–III[1–3] we perform classical trajectory calculations with a Hamiltonian in reduced form. At first, we consider the formation of a linear adduct from an atom and a linear species. We choose a center-of-mass coordinate system and employ a potential energy $V(r,\gamma)$ of the type

$$V(r,\gamma)=D\{\exp[-2\beta(r-r_e)]-2\exp[-\beta(r-r_e)]\}+A_1[(1-\cos\gamma)/2]\exp[-2\alpha(r-r_e)], \quad (2.1)$$

where r is the distance between the centers of mass of the two combining species, γ denotes the angle between the line connecting the centers of mass and the axis of the linear species, r_e is the value of r in the equilibrium configuration, β is the Morse parameter, D is the Morse dissociation energy of the adduct, and α is the ''looseness parameter'' of the anisotropy of the potential in the sense used in the original version of the SACM.[5]

The parameter A_1 can be understood as an ''anisotropy amplitude'' (at $r=r_e$). While the attraction between the two species in Eq. (2.1) is assumed to be of the simple Morse type, the anisotropy of the potential is characterized by r-dependent quanta $\epsilon(r)$ of the adduct bending vibration of the approximate form

$$\epsilon(r)=\epsilon(r_e)\exp[-\alpha(r-r_e)]. \quad (2.2)$$

This form was initially suggested by bond energy–bond order arguments[23] and generalized in the empirical exponential eigenvalue interpolation of the original version of the SACM.[5] A simple SACM analysis of a series of high-pressure recombination rate constants[9] led to the result that $\alpha/\beta\approx 0.5$. Apparently there is a fairly uniform general anisotropy present in many valence systems. Quantum-chemical calculations (see e.g., Ref. 24) confirmed the order of magnitude of α/β although often slightly larger values of the ratio α/β were found, being near to 0.6.

The parameter A_1 is related to the moment of inertia I of the linear fragment and the bending quantum $\epsilon(r_e)$ of the adduct in its equilibrium configuration. For the potential (2.1), the frequency $\omega(r_e)=\epsilon(r_e)/\hbar$ of the bending vibration of the adduct at $r=r_e$ is equal to

$$\omega(r_e)=\sqrt{\frac{A_1}{2}\left(\frac{1}{I}+\frac{1}{\mu r_e^2}\right)}, \quad (2.3)$$

where μ denotes the reduced mass of the two fragments. In practice, one often has $\mu r_e^2 \gg I$ (e.g., for NO_2 one would have $B_e=\hbar^2/2\mu r_e^2=hc\cdot 0.422\ \mathrm{cm}^{-1}$ and $B=\hbar^2/2I=hc\cdot 1.704\ \mathrm{cm}^{-1}$). Equation (2.3) then simplifies to

$$A_1\approx 2I[\omega(r_e)]^2=\frac{2I}{\hbar^2}[\epsilon(r_e)]^2=\frac{[\epsilon(r_e)]^2}{B}, \quad (2.4)$$

where B (in energy units) denotes the rotational constant of the linear fragment. Since adiabatic channel maxima are located at relatively large r values, we use Eq. (2.2) and we relate $\epsilon(r_e)=\hbar\omega(r_e)$ with the parameter A_1 through Eq. (2.4).

Equation (2.1) corresponds to the formation of a linear adduct with $\cos\gamma$ anisotropy of the bending potential and Morse-type attraction; hence, an anisotropy of the ion–dipole type is employed. In addition to this simplest case, we have also considered a series of other potentials. For example, we have studied the formation of nonlinear adducts. For this purpose, we have replaced Eq. (2.1) by

$$V(r,\gamma)=D\{\exp[-2\beta(r-r_e)]-2\exp[\beta(r-r_e)]\}+A_2[3(\cos^2\gamma)/2-q\cos\gamma+q^2/6]\times\exp[-2\alpha(r-r_e)], \quad (2.5)$$

where q is in the range $0\leqslant q<3$. The parameter q is related to the angle γ_e of the potential minimum by

$$q=3\cos\gamma_e. \quad (2.6)$$

In the equilibrium configuration $(r=r_e)$, potential maxima of the magnitude $A_2(3/2-q+q^2/6)$ at $\gamma=0$ and $A_2(3/2+q+q^2/6)$ at $\gamma=\pi$ are obtained. The bending frequency $\omega(r_e)=\epsilon(r_e)/\hbar$ now is given by

$$\omega(r_e)=\sqrt{3A_2(1/I+1/\mu r_e^2)}\sin\gamma_e \quad (2.7)$$

such that, instead of Eq. (2.4), one has

$$A_2\approx\frac{[\epsilon(r_e)]^2}{6B}\left[\frac{1}{\sin^2\gamma_e}\right]. \quad (2.8)$$

Next we have considered the formation of linear adducts with an anisotropy varying between $\cos\gamma$ and $\cos^2\gamma$ type. For these investigations, we used the potential

$$V(r,\gamma)=D\{\exp[-2\beta(r-r_e)]-2\exp[-\beta(r-r_e)]\}+A_2[3(\cos^2\gamma)/2-q\cos\gamma+q-3/2]\times\exp[-2\alpha(r-r_e)] \quad (2.9)$$

with $q\geqslant 3$. This potential in the equilibrium configuration $(r=r_e)$ has a maximum of $2qA_2$ at $\gamma=\pi$; the parameter q determines the relative contribution of $\cos^2\gamma$ and $\cos\gamma$ terms, the pure $\cos\gamma$ potential being reached at $q\to\infty$ while a purely quartic potential near $\gamma=0$ is realized at $q\to 3$. The bending frequency $\omega(r_e)=\epsilon(r_e)/\hbar$ now is given by

$$\omega(r_e)=\sqrt{A_2(q-3)(1/I+1/\mu r_e)} \quad (2.10)$$

such that, instead of Eq. (2.4), one has

$$A_2\approx\frac{[\epsilon(r_e)]^2}{2B}\left[\frac{1}{q-3}\right]. \quad (2.11)$$

On the basis of the described potentials, we employ the inverse Morse parameter as our length unit $l_u=\beta^{-1}$; kT is used as the energy unit $E_u=kT$; with the moment of inertia I of the linear fragment, a time unit $t_u=(2I/kT)^{1/2}$ is defined; $m_u=2I\beta^2$ provides a mass unit. The reduced Hamiltonian $h=H/E_u$, e.g., for the potential of Eq. (2.1), is then written as

$$h=j^2+p^2/2M+d\{\exp[-2(\rho-\rho_e)]-2\exp[-(\rho-\rho_e)]\}$$
$$+a_1[(1-\cos\gamma)/2]\exp[-(2\alpha/\beta)(\rho-\rho_e)], \qquad (2.12)$$

where j is the reduced angular momentum of the linear rotor and p the reduced momentum of relative translation. The effective mass M of the system is given by

$$M=\frac{\mu}{m_u}=\frac{\mu}{2I\beta^2}=\frac{\mu r_e^2}{I}\left[\frac{1}{2(\beta r_e)^2}\right]=\frac{B/B_e}{2(\beta r_e)^2} \qquad (2.13)$$

with $B_e=\hbar^2/2\mu r_e^2$. Furthermore, one has $\rho=r/l_u=\beta r$, $\rho_e=r_e/l_u=\beta r_e$, $d=D/E_u=D/kT$, and $a_1=A_1/E_u=A_1/kT$. Analogous relations were obtained for the other potentials with $a_2=A_2/kT$.

The capture rate constant $k_{\rm cap}$ can be expressed with the reduced and thermally averaged capture cross-section $\langle\sigma\rangle$ (in units of β^{-2}) via

$$k_{\rm cap}=\sqrt{\frac{8\pi kT}{\mu}}\frac{\langle\sigma/\pi\rangle}{\beta^2}. \qquad (2.14)$$

In the following, for convenience, we represent $\langle\sigma/\pi\rangle=k_{\rm cap}/\beta^{-2}\sqrt{8\pi kT/\mu}$ as a function of the parameters M, ρ_e, d, α/β, and a_1 (or q and a_2 instead of a_1). We concentrate our attention in particular on the thermal rigidity factors $f_{\rm rigid}$ which are defined by

$$f_{\rm rigid}=k_{\rm cap}/k_{\rm cap}(a_1=0) \qquad (2.15)$$

(or $a_2=0$), i.e., by the ratio of the capture rate constants in the presence and absence of anisotropy, the latter case corresponding to phase space theory, see below.

The extent of adiabaticity of the linear rotor (rotational period $t_{\rm rot}$) during the collision (collision time $t_{\rm col}$) can be characterized[25] by the Massey parameter $\xi=t_{\rm col}/t_{\rm rot}$ which is related to the effective mass M by

$$\xi=\sqrt{2M}. \qquad (2.16)$$

Adiabatic behavior corresponds to $\xi\gg1$ and nonadiabatic (sudden) behavior to $\xi\ll1$. For the present situation, we show that deviations from adiabatic dynamics only become apparent when ξ is much smaller than unity.

III. HARMONIC OSCILLATOR APPROXIMATION

Following earlier treatments in Refs. 3 and 11, in the present study we also compare adiabatic capture rate constants from classical trajectory calculations with results from a simple classical harmonic oscillator approximation of SACM. Adiabatic channel potential curves in reduced form, for the linear adduct potential of Eq. (2.12), are given by

$$u(\lambda)=\lambda^2/4d-\lambda+v\sqrt{2\lambda\delta} \qquad (3.1)$$

(at large λ and assuming $2\alpha/\beta=1$) where λ and δ correspond to $\lambda=2d\exp[-(2\alpha/\beta)(\rho-\rho_e)]$ and $\delta=a_1/4d$ with the symbols defined for Eq. (2.12); v denotes the quantum number of the bending vibration in the anisotropy potential. (For more details, see the analogous cases treated in Ref. 3). The reduced centrifugal energy, added to Eq. (3.1), is equal to $l^2/2M\rho^2=eb^2/\rho^2$ where l is the reduced angular momentum, e is the reduced collisional energy, and b is the reduced impact parameter. The reduced and thermally averaged cross section then follows as

$$\langle\sigma\rangle/\pi=\int_0^{v_{\max}}v\,dv\int_0^{\infty}e[b(e,f)]^2\exp(-e-e_f)de \qquad (3.2)$$

with $f=v\sqrt{\delta}$ and entrance channel energies e_f; $v_{\max}$ indicates the maximum vibrational quantum number for bonding channel potentials; at $v>v_{\max}$, channel potentials become repulsive. It is easy to show that

$$v_{\max}=(4/3)\sqrt{d/3\delta}. \qquad (3.3)$$

$b(e,f)$ in Eq. (3.2) denotes the maximum impact parameter at a given e and f, for which capture can occur, i.e., for which $\rho=\rho_e$ can be reached classically. With the present potential and centrifugal energy, $b(e,f)$ can only be calculated numerically and inserted into Eq. (3.2) which was done in this work. The results are compared with trajectory calculations in Sec. IV.

Even without evaluating $\langle\sigma\rangle/\pi$ explicitly, an important general result can be derived. Replacing v by $f=v\sqrt{\delta}$, Eq. (3.2) becomes

$$\langle\sigma\rangle/\pi=\delta^{-1}\int_0^{f_{\max}}f\,df\int_0^{\infty}e[b(e,f)]^2\exp(-e-e_f)de. \qquad (3.4)$$

As a consequence, one predicts that $k_{\rm cap}$ and the rigidity factor $f_{\rm rigid}$, for the linear adduct, become inversely proportional to δ and hence to A_1, i.e.,

$$f_{\rm rigid}\propto\frac{1}{A_1}. \qquad (3.5)$$

(One should note that this prediction only applies when $\delta\gg1$.) Equation (3.5) confirms earlier results from more approximate oscillator models.[11] The rigorous relation between $f_{\rm rigid}$ and A_1 will be determined in Sec. IV.

IV. CAPTURE RATE CONSTANTS FROM CLASSICAL TRAJECTORY CALCULATIONS: LINEAR ADDUCTS

Classical trajectory calculations were performed such as described in Refs. 1–3. About 10^4 trajectories were investigated for each $\{M,\rho_e,d,a,\alpha/\beta\}$ parameter combination (a stands for a_1 or a_2). Because the used potentials contain a repulsive component, the capture condition for a trajectory had to be changed against that used in parts I–III: Capture in the present work was assumed to be achieved when $r<r_e$ was reached. In some cases, when $r<r_e$ was not accessible, also reaching a range with oscillatory motion in r was taken as evidence for capture. A first series of calculations, for linear adducts with the potential of Eq. (2.1) and $\alpha/\beta=0.5$, was done in the adiabatic range ($M=100$), inspecting the dependence of $\langle\sigma\rangle/\pi$ on $\rho_e=\beta r_e$. Besides the dependence on ρ_e, we consider the dependence on the anisotropy which we characterize by the reduced parameter[11]

$$C=[\epsilon(r_e)]^2/2BD. \qquad (4.1)$$

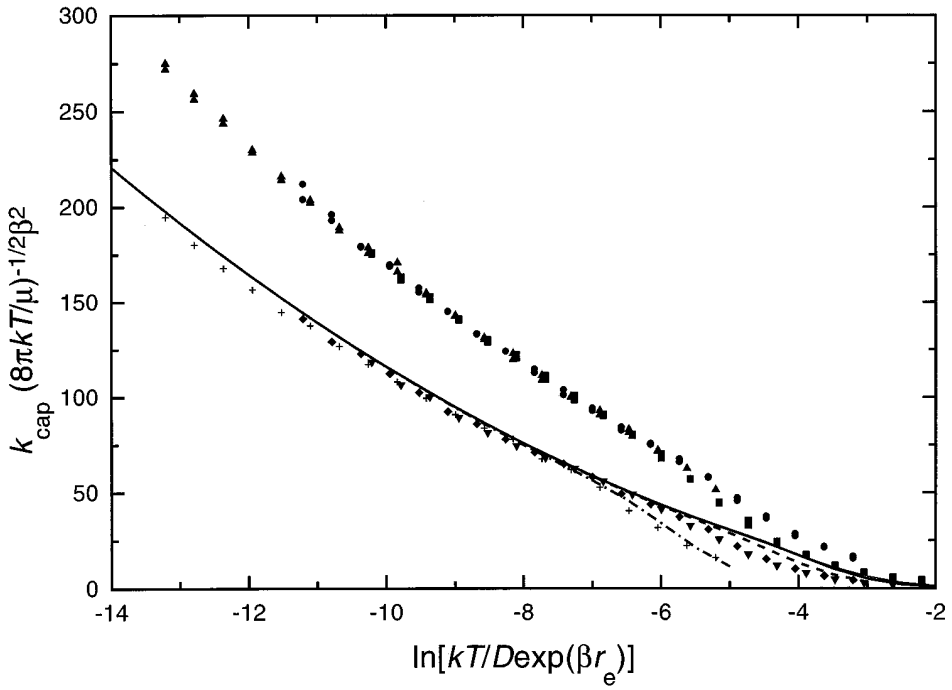

FIG. 1. Thermal capture rate constants k_{cap} for the potential of Eq. (2.1) with $\alpha/\beta=0.5$; dependence on βr_e (see text), points: classical trajectory calculations, lines: harmonic oscillator SACM; upper set: isotropic potential with $C=0$ (PST), lower set: anisotropic potential with $C=2$, see Eq. (4.1); ■ and ▼: $\beta r_e=1$, ● and ♦: $\beta r_e=2$, ▲ and +: $\beta r_e=4$; lines from bottom to top: complete Morse potential ($\beta r_e=4$, -·-·-), complete Morse potential ($\beta r_e=2$, ----), Morse potential without repulsive term (———), complete Morse potential ($\beta r_e=1$, thin full line in lower right corner).

For the potential of Eq. (2.1), according to Eq. (2.4) C is equal to $A_1/2D$ or $a_1/2d$. Calculations for $C=0$, i.e., in the absence of an anisotropy of the potential, correspond to phase space theory (PST), see, e.g., Ref. 18. Figure 1 shows representative results. One observes that $\langle\sigma\rangle/\pi = k_{cap}(8\pi kT/\mu)^{-1/2}\beta^2$ is almost a unique function of the variable $kT/[D\exp(\beta r_e)]$. Only at the highest temperature, when the repulsive part of the potential matters, deviations occur for $\beta r_e=1$ (a case which in practice is rare). The capture rate constant decreases with increasing C; i.e., in-

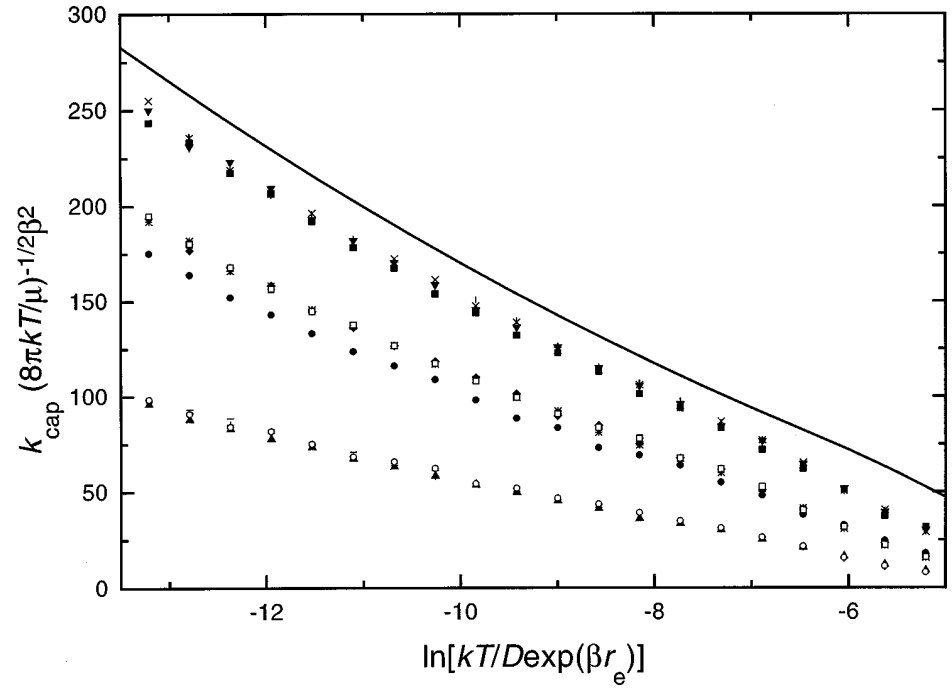

FIG. 2. Thermal capture rate constants k_{cap} for the potential of Eq. (2.1) with $\alpha/\beta=0.5$: dependence on the effective mass M in the near-adiabatic range [see text; $\beta r_e=4$; full line on top: $C=0$ (PST), groups of points from top to bottom: $C=1$, 2, and 4; effective mass $M=100$: |, □, and ○, $M=10$: ×, *, and –, $M=1$: ▼, ♦, and +, $M=0.1$: ■, ●, and ▲; $0.1\leqslant M\leqslant 100$ corresponds to Massey parameters $0.45\leqslant\xi\leqslant 14$, see Eq. (2.17)].

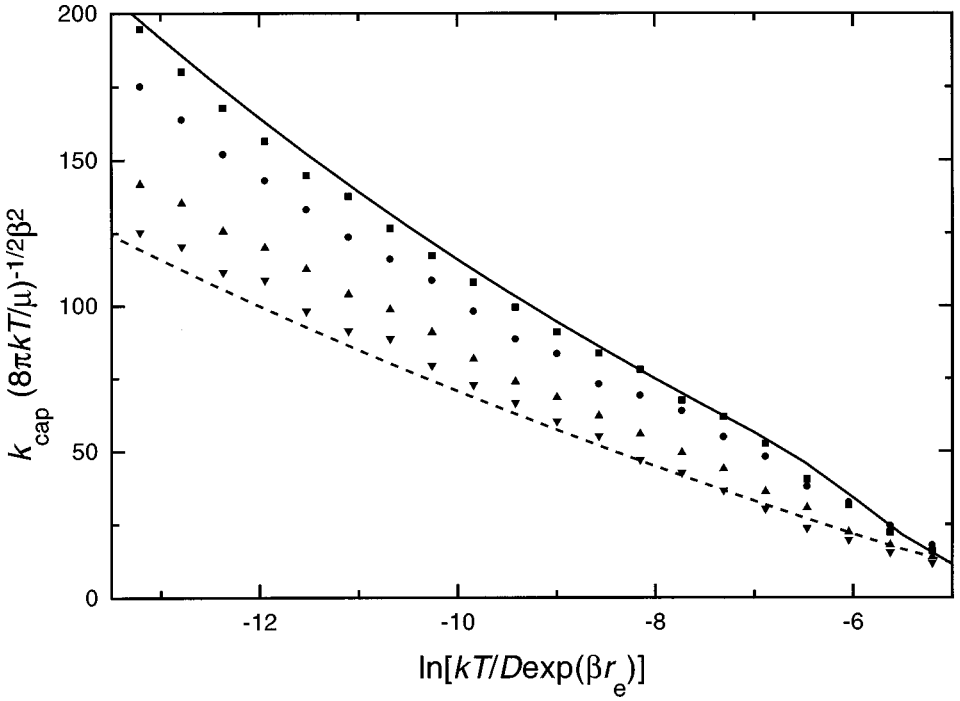

FIG. 3. Thermal capture rate constants k_{cap} for the potential of Eq. (2.1) with $\alpha/\beta=0.5$: transition from adiabatic to nonadiabatic (sudden) dynamics, see text. ($\beta r_e=4$, $C=2$; full line at the top: harmonic oscillator SACM for the adiabatic limit, see Fig. 1; points: CT from top to bottom with $M=100$ (■), 0.1 (●), 0.01 (▲), and 10^{-10} (▼), i.e., $\xi=14.1$, 0.45, 0.14, and 1.4×10^{-5}, respectively; dashed line at the bottom: analytical calculation for the sudden limit, see text).

creasing anisotropy of the potential introduces ''rigidity,'' represented by a thermal rigidity factor f_{rigid} smaller than unity.[11] Again one observes deviations from a common curve only at the highest temperatures when the repulsive term of the potentials matters. In contrast to the $C=0$ curve, here deviations are strongest for $\beta r_e=4$. Figure 1, for the case $C=2$, also includes a comparison of the trajectory results with the classical harmonic oscillator model described in Sec. III, four curves are shown: the full line corresponding to a Morse potential omitting the repulsive term (this curve practically coincides with that of a complete Morse potential and $\beta r_e=1$), the dashed curve for a complete Morse potential and $\beta r_e=2$, and the dash-dotted curve with a complete Morse potential and $\beta r_e=4$. The general agreement between the CT and approximate oscillator (SACM) treatments is very good, only minor deviations being observed as a consequence of slightly different capture criteria, particularly for high temperatures where the repulsive part of the potential matters most (overcoming of the channel maxima was the criterion in the SACM oscillator model treatment).

Choosing $\beta r_e=4$ for reference, the dependence of $\langle\sigma\rangle/\pi$ on the effective mass M (or the corresponding Massey parameter ξ) and on the anisotropy parameter C is demonstrated in Fig. 2. Only small dependences on M are noted between 0.1 and 100, being most pronounced for $C=2$. Apparently, over the shown range of effective masses $0.1\leqslant M\leqslant100$, which correspond to Massey parameters $0.45\leqslant\xi\leqslant14$, adiabatic dynamics is realized. Like in Fig. 1, $\langle\sigma\rangle/\pi$ decreases below the PST result (full line) with increasing anisotropy, i.e., when C exceeds unity.

In order to inspect the transition from adiabatic ($M\rightarrow\infty$) to nonadiabatic (sudden) dynamics ($M\rightarrow0$), we did calculations with further reduced M values. Figure 3 shows the results for $C=2$. The transition occurs between $M=0.1(\xi=0.45)$ and $M=0.01(\xi=0.14)$. Rate constants in the sudden limit $M\rightarrow0$ are 2/3 of the limiting adiabatic values (at low temperatures). Figure 3 also includes a comparison of CT and analytical results for $M\rightarrow0$, obtained for frozen orientations of the linear species and subsequent averaging over all orientations. The agreement between the two treatments of the limiting sudden dynamics is quite satisfactory.

In the following we do not further consider the transition between sudden and adiabatic dynamics, but only analyze the practically most relevant adiabatic situation. Analytical representations of the dependences of k_{cap} on βr_e, D/kT, and C were derived for $M=100$. Figure 4, as an example, for $M=100$ and $\alpha/\beta=0.5$ shows the quality of fits of k_{cap} as a function of $kT/[D\ \exp(\beta r_e)]$ and C. The capture rate constants are represented by $Y=k_{cap}(8\pi kT/\mu)^{-1/2}\beta^2$ as a function of $X=\ln(kT/D)-\beta r_e$. As demonstrated in Fig. 4, the results can be expressed very well as

$$Y(X)=\alpha_1+\alpha_2X+\alpha_3X^2. \tag{4.2}$$

Except for the high-temperature ends of the curves (for $\beta r_e=1$), where the repulsive part of the potential produces additional dependences on βr_e (see below), the fit parameters of $Y(x)$ only depend on C. Examples of fit parameters are given in Table I.

For cases with small βr_e and large kT/D, an extension of the fit is required. In this case, we employed

$$Y=\beta_1\ \sin[\pi(X-\beta_2)/\beta_3]+\beta_4+\beta_5X+\beta_6X^2. \tag{4.3}$$

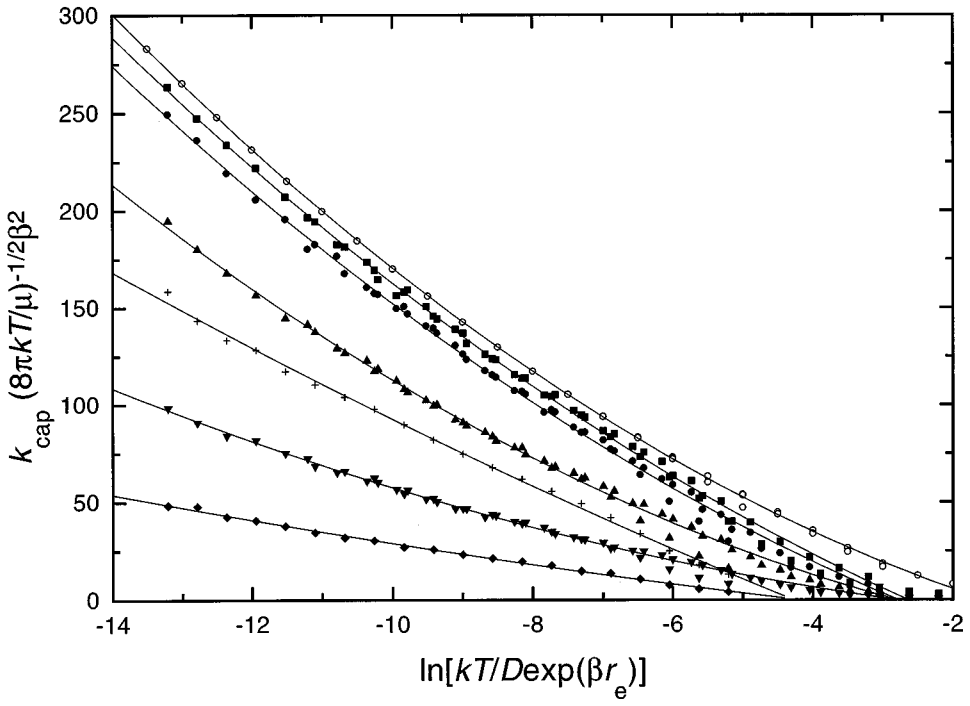

FIG. 4. Thermal capture rate constants k_{cap} for the potential of Eq. (2.1) with $\alpha/\beta=0.5$: CT results and their fit by Eq. (4.2) (examples for $\beta r_e=1$, 2, 4 and $M=100$; $C=0$ (PST), 0.5, 1, 2, 2.5, 4, and 8 from top to bottom).

As an example, for $\beta r_e=1$, Table II gives fit parameters as a function of C [here using $X=\ln(kT/D)$].

An alternative representation is provided by separate fits of the capture rate constants from phase space theory k_{cap}^{PST} and of the thermal rigidity factors $f_{rigid}(T)$ defined by Eq. (2.15), i.e.,

$$k_{cap}=f_{rigid}(T)k_{cap}^{PST}. \tag{4.4}$$

k_{cap}^{PST} is expressed with the fit parameters of Tables I and II for $C=0$. Figure 5 (for $\beta r_e=4$ and $\alpha/\beta=0.5$) shows $f_{rigid}(T)$ as a function of $\ln(kT/D)$ and of C. One observes that $f_{rigid}(T)$ at lower temperatures is practically temperature independent; for higher temperatures, a minor decrease of $f_{rigid}(T)$ is observed.

In the low-temperature range, the dependence of f_{rigid} on the anisotropy of the potential can be very well represented analytically by the expression

$$f_{rigid}(T\to 0)\approx(1+Z^2+Z^8)^{-1/8}, \tag{4.5}$$

TABLE I. Fit parameters α_i in Eq. (4.2) for thermal capture rate constants calculated with the potential of Eq. (2.1) [anisotropy parameter C from Eq. (4.1)].

C	α_1	α_2	α_3
0	−15.7706	−8.6364	0.9975
0.5	−36.5761	−11.6146	0.8305
1	−35.3951	−10.3463	0.8409
2	−20.0489	−4.7740	0.8501
2.5	−56.9892	−12.0888	0.2863
4	−10.4879	−2.5247	0.4264
8	−15.4267	−3.1423	0.1288

with $Z=C/\sqrt{2}$ or $Z=(A_1/D)^n/\gamma_1$ where $n=1$ and $\gamma_1=\sqrt{8}$. For $f_{rigid}\leqslant 0.8$, this simplifies to $f_{rigid}\approx 1/Z$ or

$$f_{rigid}\approx 2\sqrt{2}BD/[\epsilon(r_e)]^2\approx\sqrt{2}/C. \tag{4.6}$$

The rigidity factor, hence, can be expressed in a simple way by a combination of molecular parameters. The present conclusions from trajectory calculations fully confirm earlier more approximate results[11] which, by a simplified SACM treatment, led to a rough estimate of f_{rigid} (at $f_{rigid}<0.8$) of $f_{rigid}=1/C$. The new Eqs. (4.5) and (4.6) supersede this oversimplified result. Figure 6 demonstrates the fit of the calculated low-temperature rigidity factors by Eq. (4.5). It also shows the excellent performance of Eq. (4.6) for $f_{rigid}\leqslant 0.8$.

A temperature-independent rigidity factor $f_{rigid}(T)$ from Eq. (4.4) would lead to identical temperature dependences of k_{cap} and k_{cap}^{PST}. However, in real systems the high-temperature decrease of $f_{rigid}(T)$ at $\ln[kT/D\exp(\beta r_e)]>-9$ cannot always be neglected. It could be fitted by expressions of the form

$$f_{rigid}(T)=\delta_1+\delta_2\exp(X/\delta_3), \tag{4.7}$$

where $X=\ln[kT/D\exp(\beta r_e)]$. Such fits are included in Fig. 5. The high-temperature decrease of f_{rigid} below the low temperature limit $f_{rigid}(T\to 0)$ can also be expressed in general form by

$$f_{rigid}/f_{rigid}(T\to 0)=1-0.94\exp(X/2.044), \tag{4.8}$$

with $X=\ln[kT/D\exp(\beta r_e)]$ at $C\geqslant 2$ and

$$f_{rigid}/f_{rigid}(T\to 0)=1-0.94(C/2)\exp(X/2.044) \tag{4.9}$$

TABLE II. Fit parameters β_i in Eq. (4.3) for thermal capture rate constants calculated with the potential of Eq. (2.1) (high-temperature details included, $\beta r_e=1$).

C	β_1	β_2	β_3	β_4	β_5	β_6
0	−8.75377	2.76016	3.52573	1.42352	−3.26427	1.80325
0.5	−9.39689	2.76665	3.53617	2.6172	−1.51771	1.88866
1	−8.87187	3.2177	3.72405	5.7115	0.86385	1.98657
2	−4.41999	1.24957	2.81331	−5.3147	−2.44171	1.23978
4	−3.89236	13.1667	4.2395	5.99931	2.50412	0.95012

at $0\leqslant C\leqslant 2$. Figure 7 compares the fit curves from Fig. 5 with the satisfactory general representation of Eqs. (4.8) and (4.9).

Temperature-independent low-temperature rigidity factors $f_{\text{rigid}}(T\rightarrow 0)$ would only be obtained if $\alpha/\beta=0.5$ is fulfilled, i.e., when attraction and anisotropy of the potential with increasing r ''decrease synchronously.'' Deviations of the ratio α/β from 0.5 destroy this feature; if $\alpha/\beta>0.5$, comparably stronger anisotropies are sampled by the dynamics at higher temperatures such that $f_{\text{rigid}}(T\rightarrow 0)$ [apart from the behavior described by Eqs. (4.7)–(4.9)] decreases with increasing temperature; the opposite applies for $\alpha/\beta<0.5$. We demonstrate this dependence of the capture rate constants on the ratio α/β in Figs. 8–10. The deviation of $f_{\text{rigid}}(T)$ from Eqs. (4.5) and (4.6) in the case of $\alpha/\beta\neq 0.5$ can also be represented analytically in a satisfactory manner. We do this by replacing C in Eqs. (4.5) and (4.6) by an effective C_{eff} which is related to C, α/β, and kT/D by

$$C_{\text{eff}}=CF(kT/D)^{2\alpha/\beta-1} \tag{4.10}$$

with

$$F=1+0.9(2\alpha/\beta-1)^2-0.8(2\alpha/\beta-1)^3. \tag{4.11}$$

Replacing C in Eq. (4.5) by C_{eff} from Eqs. (4.10) and (4.11) for general values of α/β, one obtains thermal rigidity factors $f_{\text{rigid}}(T\rightarrow 0)$ such as shown in Fig. 10. As explained above, f_{rigid} decreases with increasing temperature for $\alpha/\beta>0.5$ and increases for $\alpha/\beta<0.5$. Figure 10 compares the analytical results for $f_{\text{rigid}}(T\rightarrow 0)$ from Eqs. (4.1), (4.5), (4.10), and (4.11) with the true SACM results. At low temperatures, the agreement is very good. At high temperatures, the temperature dependence described by Eqs. (4.7)–(4.9) was not included in the analytical representation such that some deviations arise. If necessary this effect could also be accounted for by combining Eqs. (4.5) with Eqs. (4.7)–(4.9).

Equations (4.1), (4.5), and (4.8)–(4.11) hence provide a very quick estimate of f_{rigid} in terms of the parameters kT, D, $\epsilon(r_e)$, B, and α/β. While the first four parameters are directly available, the ratio α/β has to be determined from quantum chemistry. Apparently it is most frequently close to 0.5 (± 0.1)[24] such that it can also be estimated reasonably well without having *ab initio* results.

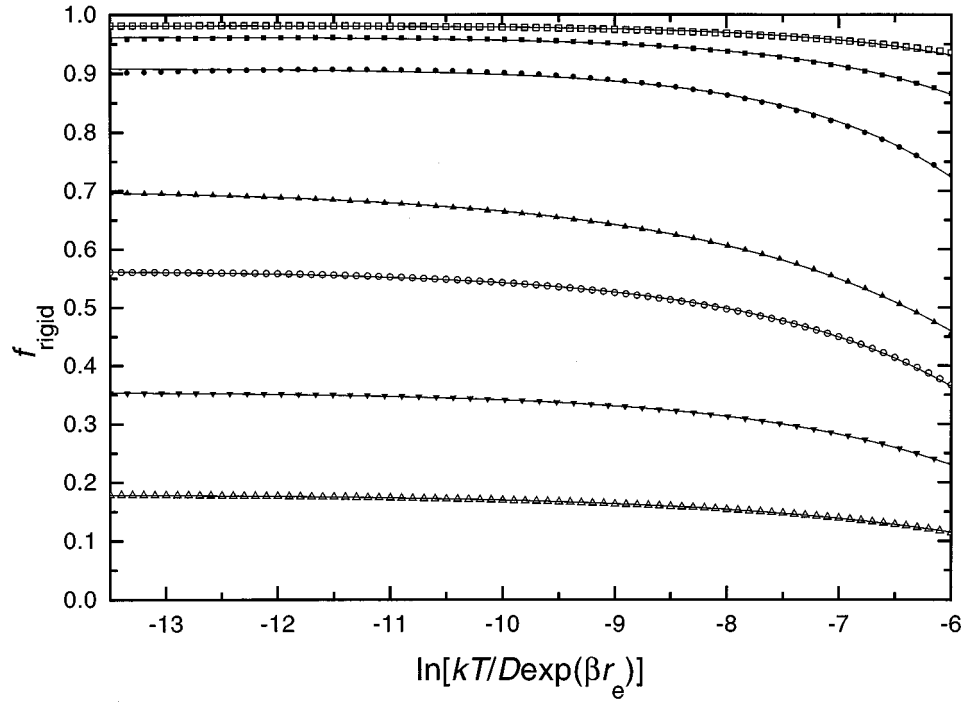

FIG. 5. Thermal rigidity factors f_{rigid} [see Eq. (4.4)] for capture calculated with the potential of Eq. (2.1) and $\alpha/\beta=0.5$ [CT results for $\beta r_e=4$; curves from top to bottom $C=0.25$ (□), 0.5 (■), 1 (●), 2 (▲), 2.5 (○), 4 (▼), and 8 (△)].

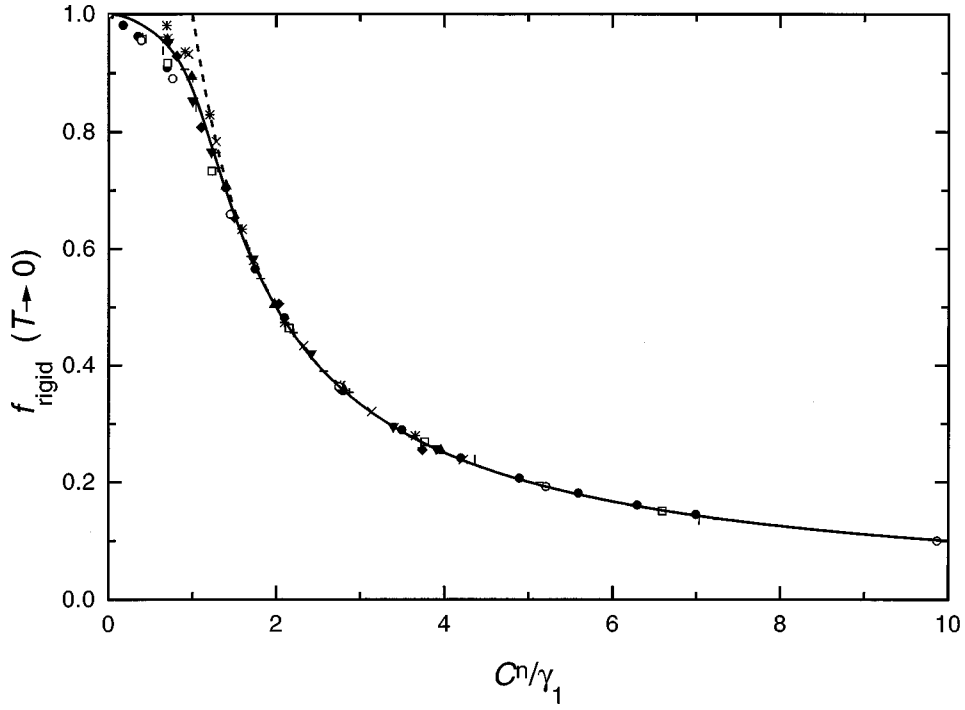

FIG. 6. Low-temperature thermal rigidity factors from Eq. (4.5) (full line) and Eq. (4.6) (dashed line) in comparison to calculated results (points) [$\alpha/\beta=0.5$; ●: linear adduct, Eq. (2.1); ▲: T-shaped adduct, Eq. (2.5) with $q=0$; ▼: nonlinear adduct, Eq. (2.5) with $q=1$; ◆: Eq. (2.5) with $q=1.5$; +: Eq. (2.5) with $q=2$; *: Eq. (2.5) with $q=3\sqrt{3/2}$; ×: Eq. (2.5) with $q=2.8$; –: linear adduct, Eq. (2.9) with $q=3$; |: Eq. (2.9) with $q=4$; □: Eq. (2.9) with $q=5$; ○: Eq. (2.9) with $q=10$; linear case: $\gamma_1=\sqrt{2}$ and $n=1$; all other cases: C replaced by (A_2/D) and γ_1 and n_1 from Eqs. (5.6) and (5.7)].

V. CAPTURE RATE CONSTANTS FROM CLASSICAL TRAJECTORY CALCULATIONS: NONLINEAR ADDUCTS

The methods described in Sec. IV next are applied to the more complicated potentials of Eq. (2.5), i.e., to potentials with nonlinear adducts. At first, the case $\alpha/\beta=0.5$ is considered. While the harmonic part of the potential of Eq. (2.1) with linear adduct formation dominated the results of Sec. IV, vibrational–rotational coupling effects become apparent with the potential of Eq. (2.5). Anharmonicity effects are

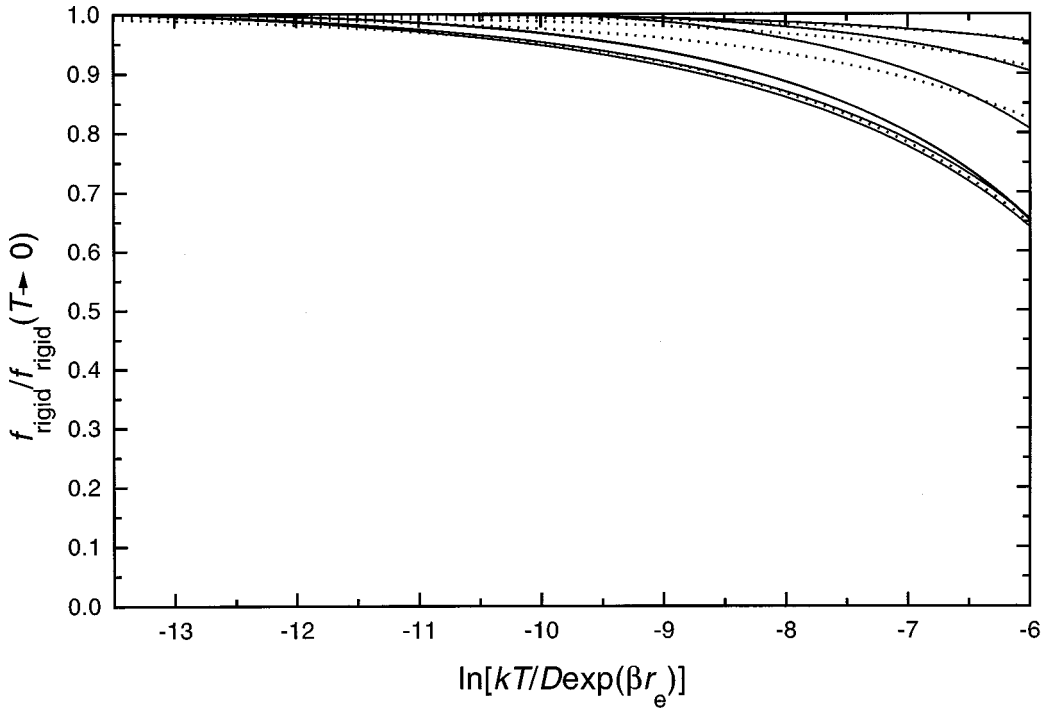

FIG. 7. Temperature dependence of rigidity factors for linear adducts, Eq. (2.1) with $\alpha/\beta=0.5$ and $\beta r_e=4$. Full lines: CT results for $C=0.25$, 0.5, 1, 2, 4, and 8 from top to bottom; dotted lines: simplified representation by Eqs. (4.8) and (4.9).

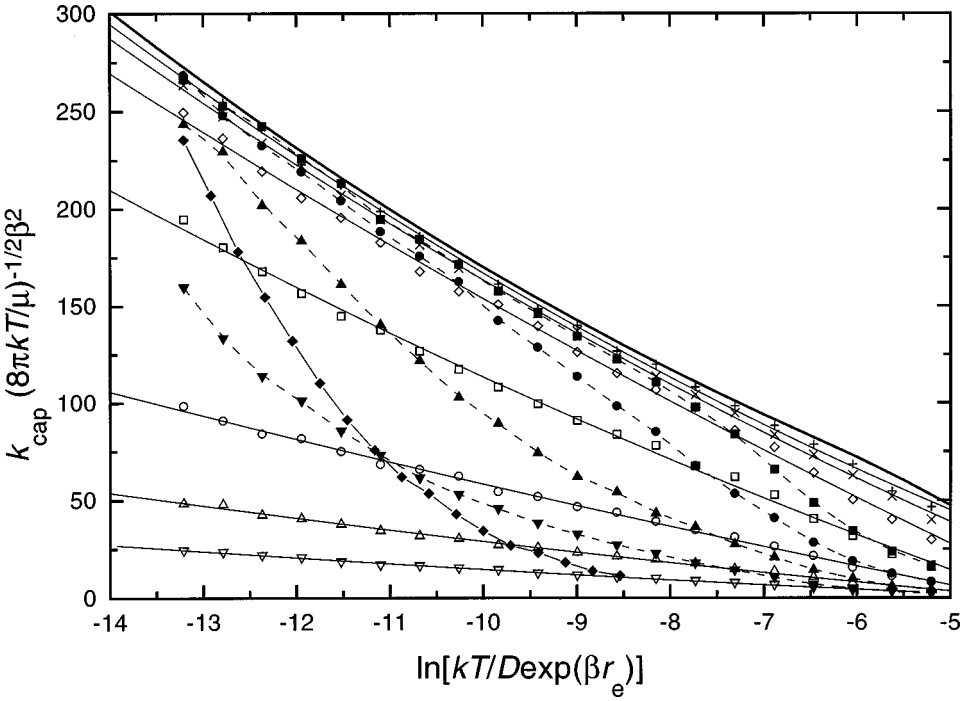

FIG. 8. Thermal capture rate constants k_{cap} for the potential of Eq. (2.1) with varying α/β. Open symbols: CT results and their fit by Eq. (4.2) for $\alpha/\beta=0.5$, $M=100$, $\beta r_e=4$, and $+(C=0.25)$, $\times(C=0.5)$, $\diamond(C=1)$, $\square(C=2)$, $\circ(C=4)$, $\triangle(C=8)$, and $\triangledown(C=16)$, line at the top: PST; closed symbols: CT results for $\alpha/\beta\neq0.5$, $\blacksquare$:$\alpha/\beta=0.6$ ($C=2$), $\bullet$:$\alpha/\beta=0.6$ ($C=4$), $\blacktriangle$:$\alpha/\beta=0.6$ ($C=8$), $\blacktriangledown$:$\alpha/\beta=0.6$ ($C=16$), $\blacklozenge$:$\alpha/\beta=0.75$ ($C=62.5$).

studied in particular with the potential of Eq. (2.9) (corresponding to linear adducts). A few representative results are illustrated in the figures; more general results are summarized in the tables and fit expressions.

Figure 11 shows thermal capture rate constants for $\alpha/\beta=0.5$ and for $q=0$ in Eq. (2.5), i.e., for T-shaped adducts with an anisotropy such as governing also even ion–quadrupole capture.[2] The full lines in the figure correspond to fits in the form of Eq. (4.2). Similarly good fits are obtained for other q values. Table III gives examples of fit parameters for a series of q values in Eqs. (2.5) and (2.9). [In Table III only calculations for $\beta r_e=4$ are included, with X

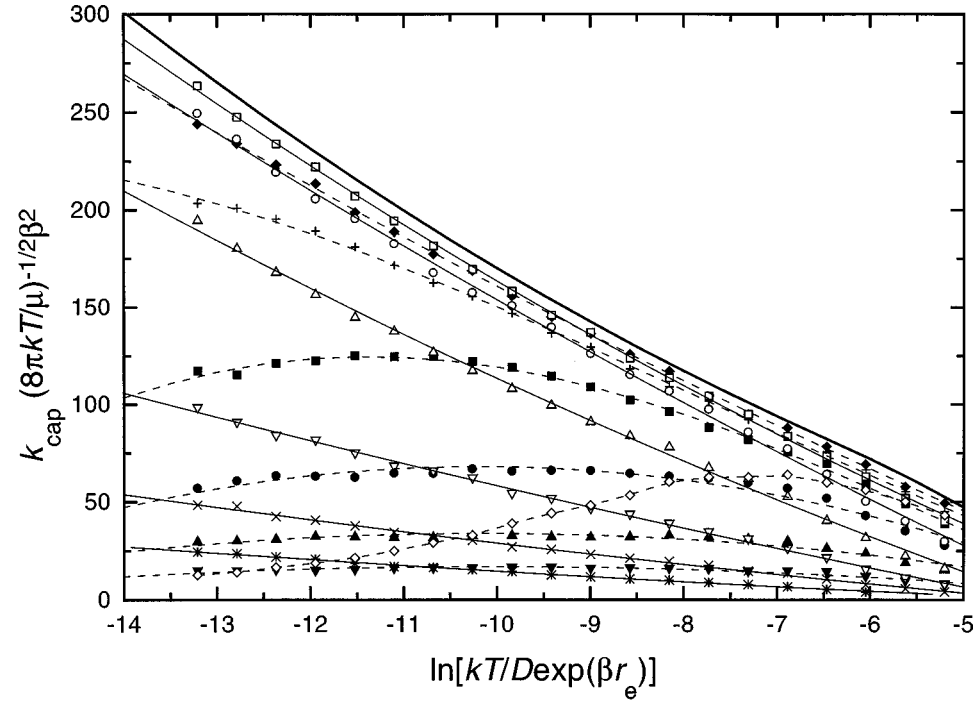

FIG. 9. Same as Fig. 8; open symbols: $\alpha/\beta=0.5$ with $C=0.5$ ($\square$), 1($\circ$), 2($\triangle$), 4($\triangledown$), 8($\times$), and 16(*); closed symbols: $\alpha/\beta=0.4$ with $C=0.125$ ($\blacklozenge$), 0.25 ($+$), 0.5 ($\blacksquare$), 1 ($\bullet$), 2 ($\blacktriangle$), and 4 ($\blacktriangledown$); $\diamond$:$\alpha/\beta=0.25$ and $C=0.25$.

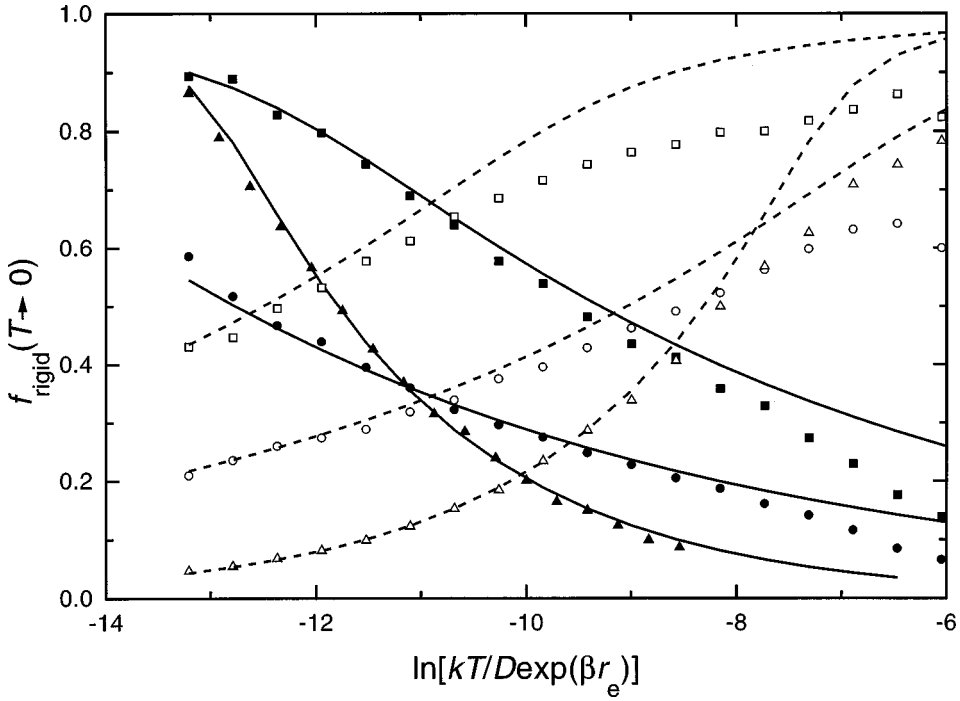

FIG. 10. Thermal rigidity factors at low temperatures for varying α/β in Eq. (2.1). Lines: representations by Eq. (4.5) with Eqs. (4.10) and (4.11). Points: CT results for $\alpha/\beta=0.75$ and $C=62.5$, (▲) $\alpha/\beta=0.6$ and $C=4$ (■) or $C=8$, (●) $\alpha/\beta=0.4$ and $C=0.25$ (□) or $C=0.5$, (○) $\alpha/\beta=0.25$ and $C=0.125$ △.

corresponding to $\ln(kT/D)$; results for other βr_e can be obtained by using $X=4-\beta r_e+\ln(kT/D)$.] The table also includes, for $0<q<3$, the equilibrium angles γ_e and the smaller and larger potential barriers of the angular potential at $r=r_e$.

The comparison of the capture rate constants with results from PST as before leads to the thermal rigidity factors. Figure 12 shows an example (for $q=0$ and $\alpha/\beta=0.5$). Again one observes nearly temperature-independent values of f_{rigid} at lower temperatures while some decrease arises at higher temperatures. The high-temperature decrease can be fitted quite similar to the results of Sec. IV. One just has to replace C in Eqs. (4.8) and (4.9) by A_2/D. Similar qualities of the fits are obtained as demonstrated in Fig. 7. We do not further

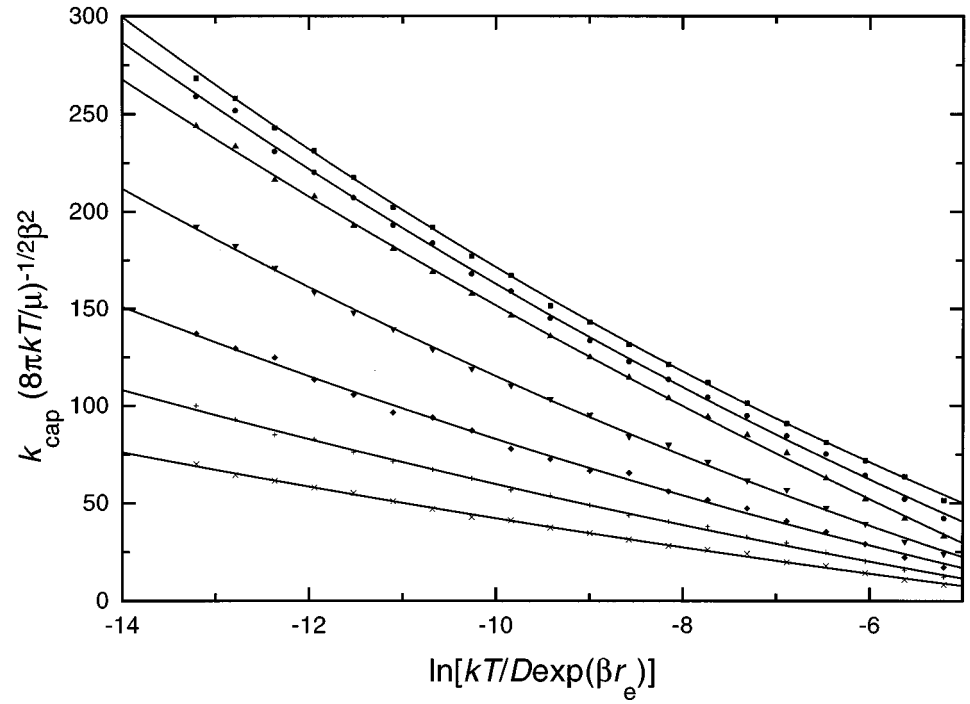

FIG. 11. Thermal capture rate constants k_{cap} for the potential of Eq. (2.5) with $\alpha/\beta=0.5$: CT results and their fit by Eq. (4.2) (examples for $\beta r_e=4$ and $M=100$; T-shaped adduct with $q=0$; A_2/D values=0, 1, 2, 4, 8, 16, and 32 from top to bottom).

TABLE III. Fit parameters α_i in Eq. (4.2) for thermal capture rate constants, calculated with the potentials of Eqs. (2.5) and (2.9) (first line with $A_2/D=0$: PST; nonlinear adducts for $0\leqslant q\leqslant 3$ with equilibrium angles γ_e (°) and angular maxima $V_{\max 1}$ and $V_{\max 2}$ at $r=r_e$; linear adducts with mixed $\cos\gamma/\cos^2\gamma$ potential for $q>3$; see text).

q	γ_e	$V_{\max 1}/D$	$V_{\max 2}/D$	A_2/D	α_1	α_2	α_3
--	--	0	0	0	31.1530	−18.1582	0.8685
	90°	1.5	1.5	1	20.4551	−19.3545	0.7260
0		3	3	2	8.2717	−20.8341	0.5111
		6	6	4	7.5691	−14.2121	0.6212
		12	12	8	6.2358	−10.2049	0.4269
	70°	1.3	5.3	2	12.2545	−18.4010	0.5902
1		2	8	3	10.6892	−15.7893	0.6067
		4	16	6	6.0333	−12.4456	0.4382
		8	32	12	4.7941	−8.6203	0.3458
	48°	0.33	8.33	2	13.2291	−14.2952	0.6495
2		0.67	16.7	4	12.6061	−10.5926	0.5713
		1.33	33.33	8	6.9216	−9.5022	0.3456
		2.67	66.7	16	3.2315	−7.9951	0.2261
	30°	0.027	5.22	1	15.4871	−15.5046	0.7781
$3^{3/2}/2$		0.054	10.4	2	12.0812	−11.5999	0.6170
		0.11	20.9	4	8.3907	−9.1273	0.4208
		0.22	41.8	8	9.0149	−5.7689	0.4283
	0°		6	1	12.3342	−14.3722	0.7283
3			12	2	9.7148	−10.0103	0.5444
			24	4	6.8744	−7.2387	0.3744
			48	8	5.2012	−4.9549	0.2808
	0°		4	0.5	8.2966	−17.9126	0.6467
4			8	1	4.4169	−12.5088	0.4869
			16	2	0.8964	−8.8056	0.2099
			32	4	1.0960	−4.7705	0.2273
	0°		5	0.25	−0.6675	−14.8738	0.4929
10			10	0.5	−1.7080	−8.8057	0.2246
			20	1	−0.2790	−4.3687	0.1403
			40	2	−0.4594	−2.3287	0.0697

analyze this part of the curves. Instead, we focus attention on the dependence of the low-temperature rigidity factors on the strength of the anisotropy and/or the molecular angle such as expressed by the parameter q in Eqs. (2.5) and (2.9). For the T-shaped adduct with $q=0$, the curve of Fig. 12 (at $f_{\text{rigid}}\leqslant 0.8$) can be well fitted by

$$f_{\text{rigid}}\approx 2^{1/4}[\sqrt{2}/(A_2/D)]^{1/2}. \tag{5.1}$$

Combining Eqs. (2.8) and (4.1) with $A_2/D=C/3$, for $q=0$, one may also express Eq. (5.1) with the quantity C from Eq. (4.1) by

$$f_{\text{rigid}}\approx 2^{1/4}3^{1/2}(\sqrt{2}/C)^{1/2}=2.06(\sqrt{2}/C)^{1/2}. \tag{5.2}$$

The exponent 1/2 of C in Eq. (5.2) corresponds to the single transitional mode of the T-shaped adduct, while the exponent unity of C in Eq. (4.6) corresponds to two transitional modes in the linear adduct. However, with increasing q more complicated expressions for f_{rigid} arise which do not follow the relation

$$f_{\text{rigid}}\propto(A_2/D)^{-b^*/2} \tag{5.3}$$

where b^* is the number of transitional modes.[11] Part of this deviation is attributed to the increasing importance of anharmonicity and vibrational–rotational coupling of the potential.

For $q=3$, i.e., a linear adduct with a quartic potential, f_{rigid} (at $f_{\text{rigid}}\leqslant 0.8$) can well be represented by

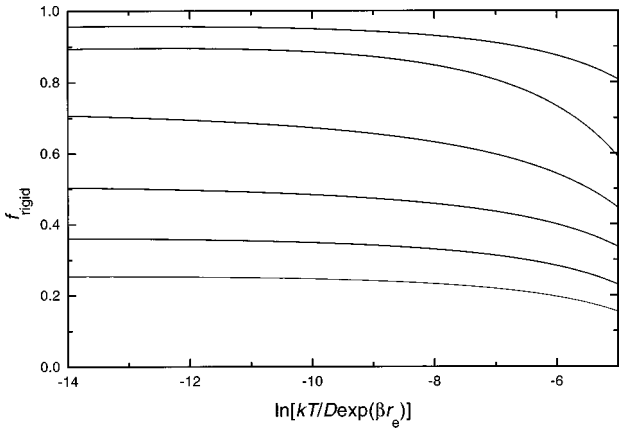

FIG. 12. Thermal rigidity factors f_{rigid} for capture calculated with the potential of Eq. (2.5) and $\alpha/\beta=0.5$ (CT results for $\beta r_e=4$ and $q=0$; curves from top to bottom $A_2/D=1$, 2, 4, 8, 16, and 32).

TABLE IV. Fit parameters γ_1 in Eq. (5.5) for low-temperature thermal rigidity factors of capture in the potentials of Eqs. (2.5) and (2.9).

q	γ_1	n
0	1.43245	0.5
1	1.40299	0.48927
1.5	1.22813	0.44276
2	1.00499	0.38396
3	0.77935	0.5
4	0.59621	0.68944
5	0.46503	0.80805
10	0.19174	0.92244

$$f_{\text{rigid}} \approx 0.65[\sqrt{2}/(A_2/D)]^{1/2}. \tag{5.4}$$

The simple relation (5.3) between the exponent $b\star$ and the number of transitional modes indeed has broken down because of the marked anharmonicity effects. Continuing the increase of q from 3 to ∞, decreasing contributions from anharmonicity in the linear adducts can be followed. A smooth transition from Eq. (5.4) to Eq. (4.6) is encountered. For a series of q values, Table III includes fit parameters α_1, α_2, and α_3 for capture rate constants expressed by Eq. (4.2) (fitting range $-14 \leqslant X \leqslant -1$ with $X = \ln kT/D - \beta r_e$).

The described rigidity factors can again be expressed in the form of Eq. (4.5) with A_1/D replaced by A_2/D from the potential of Eqs. (2.5) and (2.9). In all cases

$$f_{\text{rigid}} \approx \gamma_1 (A_2/D)^{-n} \tag{5.5}$$

provides a good representation for $f_{\text{rigid}} \leqslant 0.8$. Table IV summarizes fit parameters for a series of q values. Because of the combined contributions of anharmonicity and nonlinearity, the transition from Eq. (5.1) for a T-shaped adduct to Eq. (4.6) for a linear adduct cannot be represented in a simple way. Nevertheless, a fit is possible in the form

$$\gamma_1 = \frac{\sqrt{2} - 3.3(q/2)^6 + (\sqrt{2} + 7/q)(q/2)^8}{1 + (q/2)^8 q}, \tag{5.6}$$

$$n = 1/(1 + 1.1/q + 1800/q^6) + 10/(20 + q^3). \tag{5.7}$$

Figure 13 shows the quality of the fit expressions for γ_1 and n such as given by Eqs. (5.5)–(5.7). Figure 6 includes examples for the complete dependence of $f_{\text{rigid}}(T \to 0)$ on A_2/D. One may also represent the temperature dependence of f_{rigid} in a simple way: With the results from Table III one derives relations analogous to Eq. (4.8). One finds that $f_{\text{rigid}}/f_{\text{rigid}}(T \to 0)$ switches from an expression $1 - 0.410 \exp(X/2.359)$ for $q = 0$–2 to an expression $1 - 0.313 \exp(X/4.234)$ for $q = 2.6$–3 (with $X = \ln kT/D + 4 - \beta r_e$).

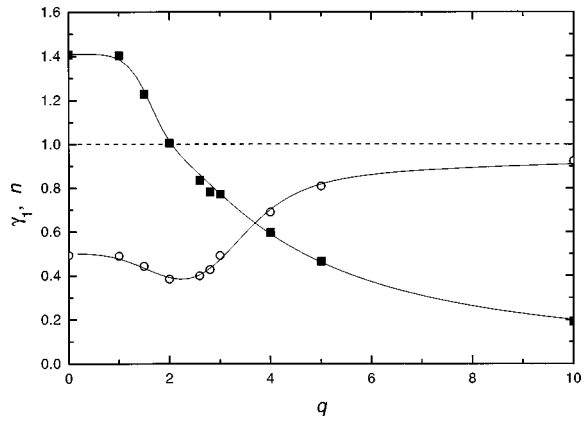

FIG. 13. Fit parameters for thermal rigidity factors in Eq. (5.5) [○: calculated n values, ■: calculated γ_1 values, full lines: Eqs. (5.6) and (5.7)].

When the ratio α/β differs from 0.5, the low-temperature rigidity factors again are no longer temperature independent. The qualitative behavior is quite similar to that shown for linear adducts in Figs. 8 and 9 such that we do not have to illustrate the effect again. Instead we give only fit parameters. To a first approximation C (or A_2/D) in Eqs. (5.1), (5.2), (5.4), and (5.5) has just to be replaced by effective values C_{eff} [or $(A_2/D)_{\text{eff}}$] such as given in Eq. (4.10). The best fits are obtained by using

$$C_{\text{eff}} = FC(kT/D)^{2\alpha/\beta - 1} \tag{5.8}$$

with

$$F = 1 - 0.4(2\alpha/\beta - 1) + 0.9(2\alpha/\beta - 1)^2 \tag{5.9}$$

for $q = 0$,

$$F = 1 - 0.7(2\alpha/\beta - 1) + (2\alpha/\beta - 1)^2 \tag{5.10}$$

for $q = 2$,

$$F = 1 - 0.7(2\alpha/\beta - 1) + 0.7(2\alpha/\beta - 1)^2 \tag{5.11}$$

for $q = 3$. Putting F simply equal to unity reproduces f_{rigid} to within $\pm 10\%$ over the range $0.4 \leqslant \alpha/\beta \leqslant 0.6$.

VI. SACM TREATMENT OF LOW-TEMPERATURE RIGIDITY FACTORS

The classical trajectory results described in the previous sections on the one hand characterize the transition from nonadiabatic (sudden) to adiabatic dynamics. On the other hand, they provide analytical expressions for capture rate constants in the adiabatic classical range. For example, Eqs. (4.5) and (4.6) provide low-temperature rigidity factors whereas Eq. (4.8) includes high-temperature effects. The given formulas allow for a quick estimate of the rigidity factors as a function of molecular parameters governing the attraction and anisotropy parts of the potential.

In the following section two additional aspects are investigated. First, the agreement between SACM and CT calculations is demonstrated for the range of adiabatic dynamics. This result is in complete analogy with parts I–III of this series.[1–3] Second, SACM expressions are derived for very low temperatures where the CT treatment becomes invalid.

Similar to the treatment of Refs. 1–4 we have calculated adiabatic channel potential curves along the reaction path r diagonalizing the Hamiltonian, e.g., Eq. (2.13). Via the channel maxima, the activated complex pseudo-partition functions and finally the capture rate constants were calculated. Figure 14 represents the results for linear adducts and $\alpha/\beta = 0.5$. The lowest set of curves (III) with the largest value of the parameter C [Eq. (4.1)] corresponds to the strongest anisotropy of the potential. In this case adiabatic zero-point barriers arise which result in an exponential decrease of k_{cap} with decreasing temperature. At high temperatures, the

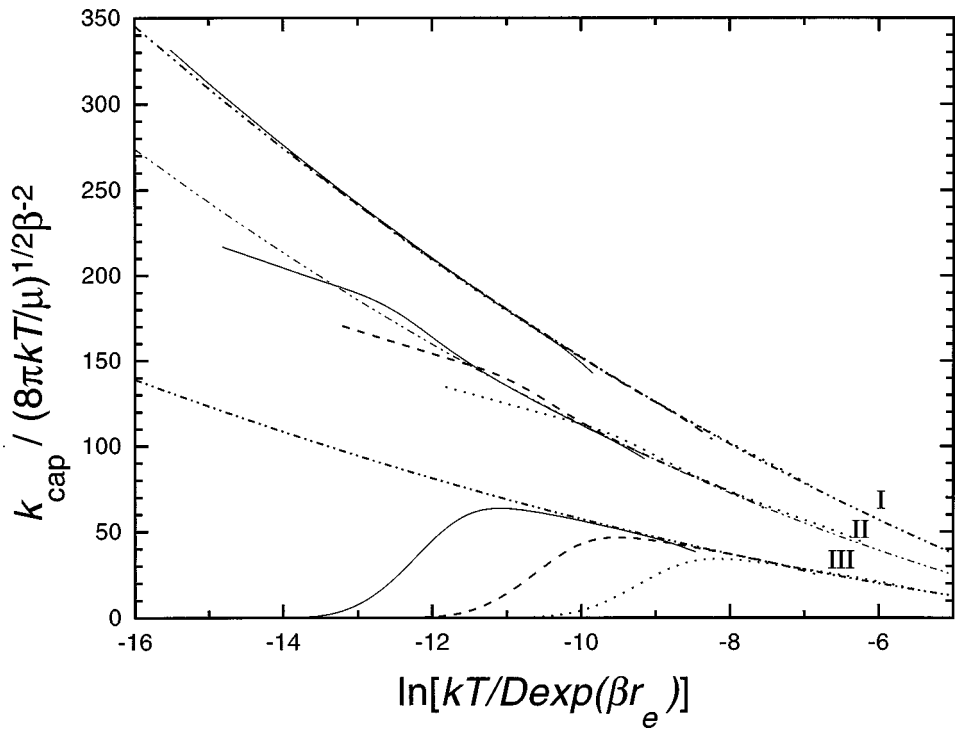

FIG. 14. Low-temperature capture rate constants from SACM calculations for the potential of Eq. (2.1) with $\alpha/\beta=0.5$ and $\beta r_e=4$ [groups of curves I: $C=1$, II: $C=2$, and III: $C=4$; $A_1 \exp(-\beta r_e)/B=183.2$ (full lines), 36.63 (dashed lines), and 9.158 (dotted lines): comparison with CT calculations (dash-dot-dotted lines)].

SACM calculations well approach the CT results (due to a limitation of the range of quantum numbers included in the SACM treatment, at the end of the calculated range one observes a decrease of the SACM values below the CT values which here is not a relevant numerical artifact). With decreasing the strength of the anisotropy (decreasing C values in groups II and I), the effect of adiabatic zero-point barriers disappears. The SACM results for k_{cap} with increasing T approach the CT results from below, overshoot, and finally approach the CT results accurately (the artifact at the high-temperature end is again visible). Figure 14 demonstrates that (apart from the described small calculational high-temperature artifact) SACM and CT results agree very well in the classical adiabatic range such as it should be and was also found in Refs. 1–3. In the quantum range, only SACM works. A plot of $k_{cap}^{SACM}/k_{cap}^{CT}$ as a function of $\ln(kT/B)$ in Fig. 15 illustrates the dominant importance of the ratio kT/B and the change of the quantum rate constant with varying anisotropy strength C.

Unlike Refs. 1–3, a rigorous analytical low-temperature limiting expression of k_{cap}^{SACM} cannot be formulated easily because the perturbation treatment cannot be elaborated explicitly. Nevertheless, approximate analytical results can be produced such as shown in the following. There are two ranges of conditions: for weak anisotropies ($C \leqslant 2$), no adiabatic zero-point barriers appear, for stronger anisotropies ($C \geqslant 2$), zero-point barriers become apparent. As long as there are zero-point barriers, they govern the limiting low-temperature rate constants. The calculated adiabatic zero-point barriers $E_0(l=0)$ ($l=$quantum number of orbital motion) can be approximated empirically by

$$\frac{E_0(l=0)}{B} \approx \frac{3}{2}\left[\frac{C-2}{C}+0.47\left(\frac{C-2}{C}\right)^{3.43}\right]^2 \quad \text{for } 2 \leqslant C \leqslant 3.2115, \tag{6.1}$$

$$\frac{E_0(l=0)}{B} \approx \frac{C-2}{4}-\frac{0.223}{C} \quad \text{for } C \geqslant 3.2115. \tag{6.2}$$

The corresponding positions $r^{\neq}$ of the channel maxima are expressed by

$$\lambda^{\neq} \approx 3(C-2+C^2/36)/C \quad \text{for } 2 \leqslant C \leqslant 3.2115, \tag{6.3}$$

$$\lambda^{\neq} \approx C^2/8+0.11 \quad \text{for } C \geqslant 3.2115, \tag{6.4}$$

where $\lambda^{\neq}$ is related to $r^{\neq}$ by

$$\beta r^{\neq} = \beta r_e - \ln[\lambda^{\neq}(B/D)/C]. \tag{6.5}$$

The resulting limiting low-temperature capture rate constants have the form

$$k_{cap}^{SACM}(T \to 0) \approx r^{\neq 2}\sqrt{8\pi kT/\mu}\, \exp[-E_0(l=0)/kT] \tag{6.6}$$

to be combined with Eqs. (6.1)–(6.5). In the ''strong-field limit'' [26] of large anisotropies ($C \gg 1$), this approaches

$$k_{cap}^{SACM}(T \to 0) \approx \beta^{-2}\sqrt{8\pi kT/\mu}[\beta r_e - \ln(B/D) - \ln(C/8)]^2 \times \exp[-(C/4-1/2)B/kT]. \tag{6.7}$$

Figure 15 compares the accurate SACM results with the sim-

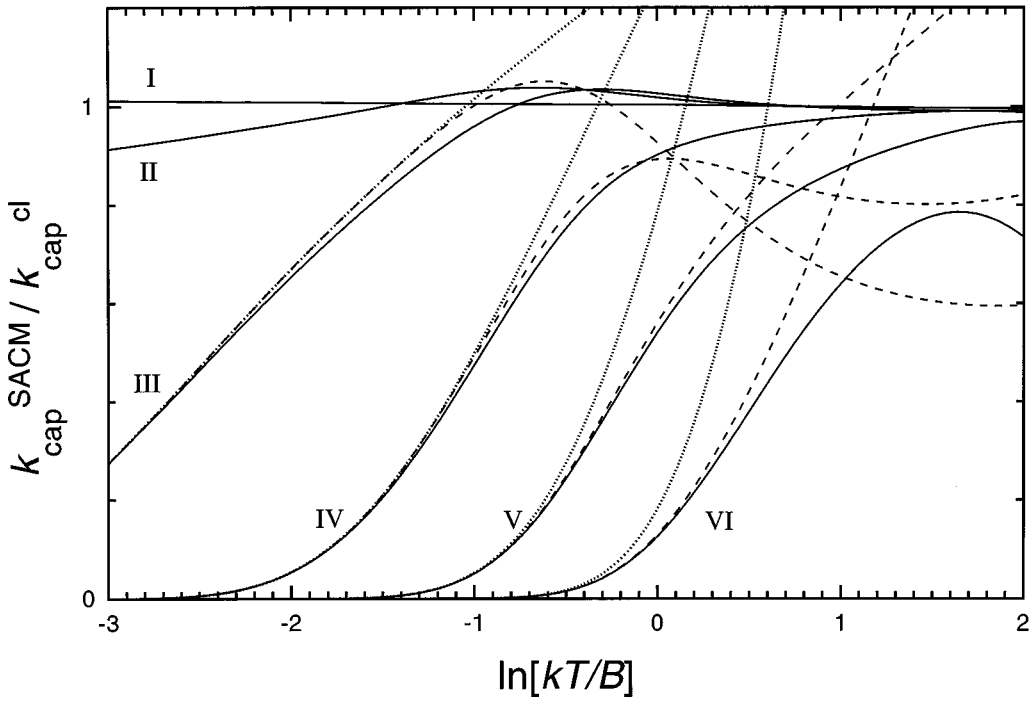

FIG. 15. Same as Fig. 14, reduced representation of capture rate constants from SACM (k_{cap}^{SACM}) and CT (k_{cap}^{cl}) [groups of curves I: $C=1$, II: $C=2$, III: $C=2.5$, IV: $C=4$, V: $C=8$, and VI: $C=16$. $A_1 \exp(-\beta r_e)/B=183.2$ (full lines); comparison with limiting low-temperature expressions from SACM, Eqs. (6.1)–(6.6) (dotted lines), and Eqs. (6.1)–(6.5), (6.8) (dashed lines)].

plified explicit results from Eqs. (6.1)–(6.6). The agreement in the limiting low-temperature behavior is excellent. One may improve the agreement for higher temperatures even more by taking into account that, for rigid situations, higher channels contribute much more strongly to the rotational partition function in the denominator of Eq. (6.6) than to the activated complex partition function of the numerator of Eq. (6.6). Replacing Eq. (6.6) by

$$k_{cap}^{SACM}(T\to 0)\approx r^{\neq 2}\sqrt{8\pi kT/\mu}\,[1+3\exp(-2B/kT)]^{-1} \times \exp[-E_0(l=0)/kT], \tag{6.8}$$

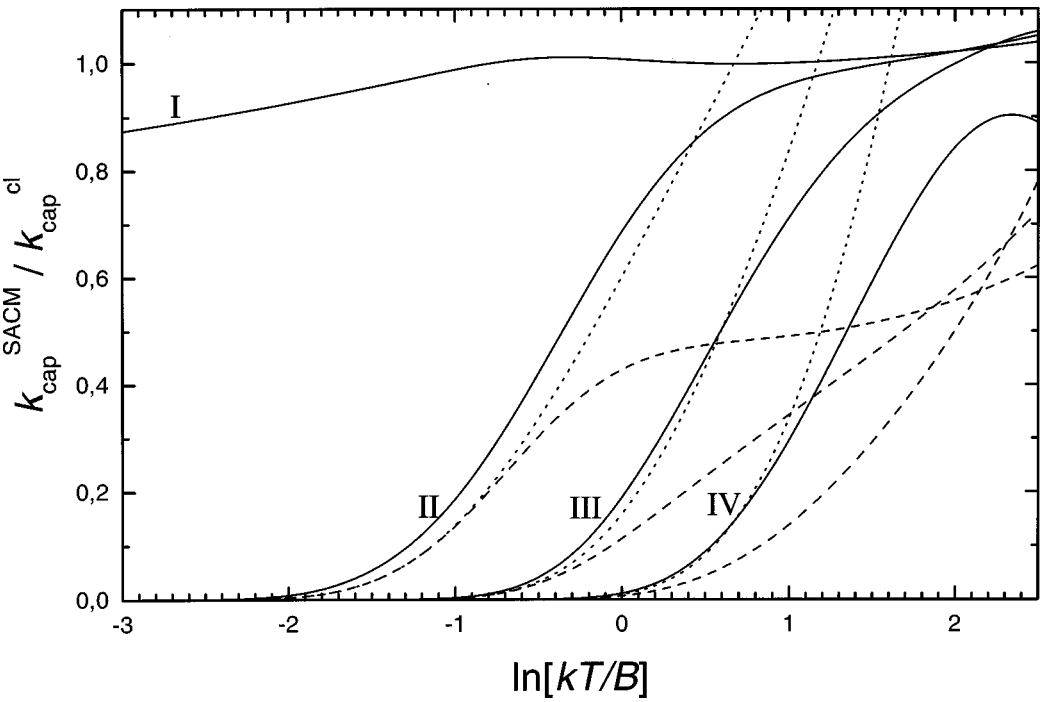

FIG. 16. Same as Fig. 15 for T-shaped adduct, Eq. (2.5) with $\alpha/\beta=0.5$, $q=0$, $\beta r_e=4$ [groups of curves I: $C=2$, II: $C=4$, III: $C=8$, and IV: $C=16$. $A_2 \exp(-\beta r_e)/B=36.63$; full lines: SACM results; dotted lines: Eqs. (6.6), (6.9)–(6.11); dashed lines: Eqs. (6.8)–(6.11)].

with $E_0(1)$ and $r^{\neq}$ from Eqs. (6.1)–(6.5), therefore, gives even better agreement, see Fig. 15. However, Eq. (6.8) can only be used for the range where k_{cap} curves up; at higher temperatures, the neglection of higher terms becomes noticeable. For the opposite case without adiabatic zero-point barriers (at $0 \leqslant C \leqslant 2$), Fig. 15 shows that k_{cap} markedly deviates from the classical value only at extremely low temperatures. In this case, however, the standard valence potential used in our work in practice becomes unrealistic since other long-range potentials dominate the capture. For this reason, we did not further investigate this limit for a Morse potential.

In the range $C>2$, the transition from the limiting low-temperature capture constants of Eqs. (6.1)–(6.7) to the classical rate constants of Eq. (4.2) cannot be so well represented in reduced form as in ion–dipole capture.[4] The overshoot of the classical capture rate constant prevents the appearance of a universal doubly reduced representation. For this reason, we do not further construct transition curves but refer to the results of Fig. 15.

Besides the SACM low-temperature quantum limit of capture forming linear adducts, we also describe results for capture forming T-shaped adducts ($q=0$). Quite similar behavior is found as for linear adduct formation. For $C \geqslant 2$, adiabatic zero-point barriers arise with

$$\frac{E_0(l=0)}{B} \approx \frac{3}{8}(C-2). \tag{6.9}$$

The corresponding positions of the channel maxima are

$$\lambda^{\neq} \approx 3C^2/6 \quad \text{for } C \geqslant 2 \tag{6.10}$$

where $\lambda^{\neq}$ is related to $r^{\neq}$ by

$$\beta r^{\neq} \approx \beta r_e - \ln[\lambda^{\neq}(B/D)/C]. \tag{6.11}$$

This leads to a capture rate constant of the form of Eq. (6.8) with $r^{\neq}$ and $E_0(l=0)$ from Eqs. (6.9)–(6.11). Figure 16 shows several examples. For the case of the T-shaped adduct, the perturbation-theoretical eigenvalues for ion–quadrupole capture[2] have been modified to derive Eqs. (6.9)–(6.11). The same procedure would also allow one to account for variations of the ratio α/β from the value 0.5 which was used in Fig. 16.

VII. CONCLUSIONS

Our present combined quantum statistical adiabatic channel and classical trajectory calculations showed again that, in the range of adiabatic dynamics, the SACM and CT treatments coincide for classical conditions. In the quantum range, only the SACM gives correct results. The transition from adiabatic to nonadiabatic dynamics was treated by CT methods.

In order to facilitate the practical application of the present study, in the following we briefly summarize the most important results of our work. We only consider the temperature range $kT/B \gg 1$ where CT results apply. For $kT/B<1$, where only SACM is valid, either the results of Sec. VII can be used or individual calculations should be made by analogy to this section.

In the range of classical adiabatic dynamics, the capture rate constant from phase space theory can be well represented by Eq. (4.2),

$$Y(X) = \alpha_1 + \alpha_2 X + \alpha_3 X^2, \tag{7.1}$$

with $Y = k_{cap}^{PST}(8\pi kT/\mu)^{-1/2}\beta^2$, $X = \ln(kT/D) - \beta r_e$, $\alpha_1 = -15.7706$, $\alpha_2 = -8.6364$, and $\alpha_3 = 0.9975$ (see Table I; some minor deviations arise for small βr_e at very high temperatures, see Eq. (4.3) and Table II).

Accounting for the anisotropy of the potential introduces thermal rigidity factors $f_{rigid} = k_{cap}/k_{cap}^{PST}$. At low temperatures (but still in the classical range), these are of the form [Eq. (4.5)]

$$f_{rigid}(T \to 0) \approx (1 + Z^2 + Z^8)^{-1/8}, \tag{7.2}$$

where $Z = (A_1/D)^n/\gamma_1$ or $Z = (A_2/D)^n/\gamma_1$. The anisotropy amplitudes A_1 or A_2 are related to the parameter [Eq. (4.1)]

$$C = [\epsilon(r_e)]^2/2BD, \tag{7.3}$$

by $A_1/2D = C$ (linear adducts) or $A_2/D = C/3\sin^2\gamma_e$ [nonlinear adducts Eqs. (2.4) and (2.9); anharmonicity effects for linear adducts are described by A_2 from Eq. (2.9)]. When the ratio α/β of the looseness parameter α and the Morse parameter β of the potential differs from the value 0.5, in Eq. (7.2) C, A_1/D, or A_2/D have to be replaced by effective values given by Eqs. (4.10) and (4.11) or Eqs. (5.8)–(5.11). The parameters n and γ_1 used in Eq. (7.2) can be well represented by Eqs. (5.6) and (5.7) as a function of the quantity q which accounts for nonlinearity and anharmonicity of the potential [see Eqs. (2.5)–(2.11)]. A high-temperature correction of the rigidity factor finally is provided by Eqs. (4.8) and (4.9), e.g., at $C \geqslant 2$ by

$$f_{rigid}/f_{rigid}(T \to 0) \approx 1 - 0.94\exp(X/2.044), \tag{7.4}$$

with $X = \ln kT/D - \beta r_e$ [for nonlinear adducts, see remarks after Eq. (5.7)].

In spite of the number of expressions to be used, the described calculation of k_{cap} is very direct and without computational effort. It is of considerable exploratory value as long as no complete and reliable potential-energy surfaces are available. Being based on systematic trajectory calculations, it provides a clear picture of the contributions of various molecular parameters to the capture rate constant.

ACKNOWLEDGMENTS

Financial support of this work by the Deutsche Forschungsgemeinschaft (SFB 357 ''Molekulare Mechanismen unimolekularer Reaktionen'') as well as by the Fund of the Promotion of Research at the Technion are gratefully acknowledged.

[1] A. I. Maergoiz, E. E. Nikitin, J. Troe, and V. G. Ushakov, J. Chem. Phys. **105**, 6263 (1996) (part I).
[2] A. I. Maergoiz, E. E. Nikitin, J. Troe, and V. G. Ushakov, J. Chem. Phys. **105**, 6270 (1996) (part II).
[3] A. I. Maergoiz, E. E. Nikitin, J. Troe, and V. G. Ushakov, J. Chem. Phys. **105**, 6277 (1996) (part III).

[4] J. Troe, J. Chem. Phys. **87**, 2773 (1987); **105**, 6249 (1996).
[5] M. Quack and J. Troe, Ber. Bunsenges. Phys. Chem. **78**, 240 (1974); **79**, 170 (1975); **79**, 469 (1975).
[6] A. I. Maergoiz, E. E. Nikitin, and J. Troe, J. Chem. Phys. **95**, 5117 (1991).
[7] A. I. Maergoiz, E. E. Nikitin, and J. Troe, Z. Phys. Chem. **172**, 129 (1991).
[8] A. I. Maergoiz, E. E. Nikitin, and J. Troe, Z. Phys. Chem. **176**, 1 (1992).
[9] C. J. Cobos and J. Troe, J. Chem. Phys. **83**, 1010 (1985).
[10] J. Troe, *22nd Symposium (International) on Combustion* (The Combustion Institute, Pittsburgh, 1988), p. 843.
[11] J. Troe, Z. Phys. Chem. NF **161**, 209 (1989).
[12] J. Troe, J. Chem. Soc., Faraday Trans. **87**, 2299 (1991).
[13] L. B. Harding, J. Phys. Chem. **93**, 8004 (1989); **95**, 8653 (1991).
[14] D. Fulle, H. F. Hamann, H. Hippler, and J. Troe, J. Chem. Phys. **105**, 1001 (1996); R. Forster, M. Frost, D. Fulle, H. F. Hamann, H. Hippler, A. Schlepegrell, and J. Troe, *ibid.* **103**, 2949 (1995); H. Hippler, M. Siefke, H. Stark, and J. Troe, *ibid.* (in press).
[15] D. L. Baulch, C. J. Cobos, R. A. Cox, P. Frank, G. Hayman, Th. Just, J. A. Kerr, T. Murrells, M. J. Pilling, J. Troe, R. W. Walker, and J. Warnatz, J. Phys. Chem. Ref. Data **23**, 847 (1994).
[16] R. Atkinson, D. L. Baulch, R. A. Cox, R. F. Hampson, J. A. Kerr, M. Rossi, and J. Troe, J. Phys. Chem. Ref. Data **26**, 521 (1997).
[17] J. Troe, J. Chem. Soc., Faraday Trans. **90**, 2303 (1994).
[18] T. Baer and W. L. Hase, *Unimolecular Reaction Dynamics. Theory and Experiments* (Oxford University Press, New York, Oxford, 1996).
[19] K. A. Holbrook, M. J. Pilling, and S. H. Robertson, *Unimolecular Reactions*, 2nd ed. (Wiley, Chichester, 1996).
[20] X. Hu and W. L. Hase, J. Chem. Phys. **95**, 8073 (1991); G. H. Peslherbe and W. L. Hase, *ibid.* **101**, 8535 (1994).
[21] M. Stumpf, A. J. Dobbyn, D. H. Mordaunt, H.-M. Keller, H. Flöthmann, and R. Schinke, Faraday Discuss. **102**, 193, (1995).
[22] A. I. Maergoiz, E. E. Nikitin, J. Troe, and V. G. Ushakov, J. Chem. Phys. (to be published) (part V).
[23] M. Jungen and J. Troe, Ber. Bunsenges. Phys. Chem. **74**, 276 (1970); H. Gaedtke and J. Troe, *ibid.* **77**, 24 (1973).
[24] L. B. Harding, R. Guadagnini, and G. C. Schatz, J. Phys. Chem. **97**, 5472 (1993); J. H. Kiefer, P. S. Mudipali, A. F. Wagner, and L. B. Harding, J. Chem. Phys. **105**, 8075 (1996); L. B. Harding, Ber. Bunsenges. Phys. Chem. **101**, 363 (1997).
[25] E. E. Nikitin and J. Troe, Ber. Bunsenges. Phys. Chem. **101**, 445 (1997).
[26] A. I. Maergoiz, J. Troe, and Ch. Weiss, J. Chem. Phys. **101**, 1885 (1994).